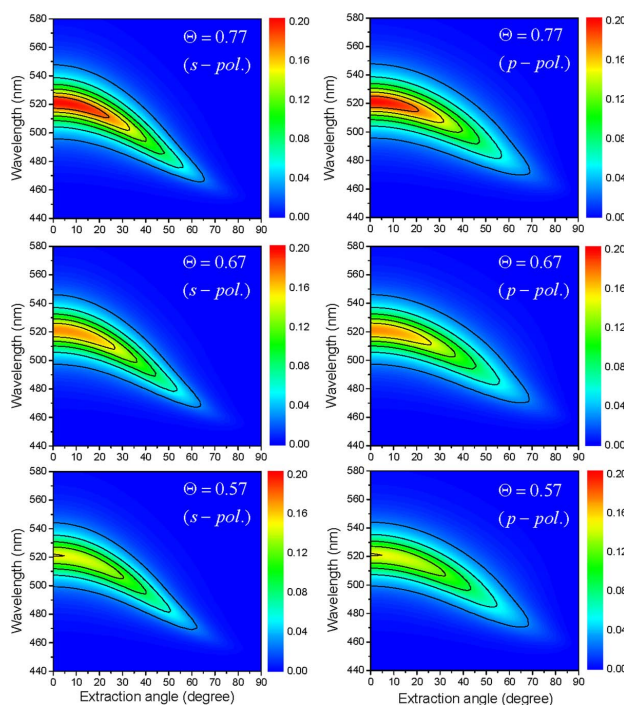# A Generalized Fabry–Pérot Formulation for Optical Modeling of Organic Light-Emitting Diodes Considering the Dipole Orientation and Light Polarization

Kyungnam Kang
Yongjeong Lee
Jungho Kim, Member, IEEE
Hyesog Lee
Byungchoon Yang

A Generalized Fabry–Pérot Formulation for Optical Modeling of Organic Light-Emitting Diodes Considering the Dipole Orientation and Light Polarization

Kyungnam Kang,[1] **Yongjeong Lee,**[1] **Jungho Kim,**[1] *Member, IEEE*,
Hyesog Lee,[2] **and Byungchoon Yang**[2]

[1]Advanced Display Research Center, Department of Information Display, Kyung Hee University, Seoul 130-701, South Korea
[2]Frontier Technology Team, Samsung Display Company, Yongin 446-711, South Korea

Abstract: The Fabry–Pérot formulation has been widely used as a simple and intuitive optical modeling method of organic light-emitting diodes (OLEDs). However, because the Fabry–Pérot formulation in the optical modeling of OLEDs does not include the effect of the dipole orientation and light polarization on light emission characteristics, rigorous electromagnetic models should be used, in spite of their heavy mathematical and computational complexity. In addition, the validity and the limitation of the Fabry–Pérot formulation for OLEDs have yet to be proven. We propose a generalized Fabry–Pérot formulation to calculate the dependence of the dipole orientation and light polarization on the angular emission characteristics using a simple analytical equation rather than a complicated electromagnetic model. The generalized Fabry–Pérot formulation is derived, together with detailed steps, and becomes equivalent to the current Fabry–Pérot formulation in isotropic dipole orientation. In addition, the physical interpretation of the proposed Fabry–Pérot formulation is elucidated in comparison with the quantum mechanical model. To demonstrate the applicability and the validity of the generalized Fabry–Pérot formulation, the angular emission spectra of a top-emitting OLED are calculated with respect to the horizontal dipole ratio and the light polarization, which can be easily calculated based on a simple analytical equation.

Index Terms: Organic light-emitting diodes (OLEDs), optical model, Fabry–Pérot formulation, dipole orientation.

1. Introduction

Optical modeling of organic light-emitting diodes (OLEDs) has been intensively studied to improve the out-coupling efficiency together with the angular emission dependence [1], [2]. Because OLEDs are composed of multiple thin films having the total thickness on the order of hundreds of nanometer, micro-cavity effect plays an important role in the light emission characteristics [3]–[6].

The orientation of a dipole emitter is also a crucial factor to determine the light emission characteristics because horizontally-oriented dipole emitters give higher out-coupling efficiency than vertically-oriented dipole emitters [7]–[9]. In addition, the angular emission characteristics depends on polarization of light [10]–[12], which should be considered for high-contrast OLEDs based on a circular polarizer. Thus, optical model of OLEDs should be able to quantify how the dipole orientation and polarization dependency affect the angular emission characteristics with respect to the wavelength.

Rigorous electromagnetic models have been proposed to calculate the effect of the dipole orientation and polarization dependency on the light emission characteristics of OLEDs [13]–[16]. Dipole emission in OLEDs was described by the classical radiation theory of an electrical dipole antenna, which was equivalent to the quantum-mechanical model of an electrical dipole transition coupled to photonic modes [13], [14]. However, this so-called power spectrum method was too complicated because it required analytical integration and the optimization of calculation parameters. Another electromagnetic model used electric-field source terms in the matrix formalism and needed no analytical integration [15], [16]. Nevertheless, this source-term method required complicated matrix calculation and could not give a good insight to the optical design of OLEDs.

Fabry–Pérot formulation, which combines Fabry–Pérot resonator theory and the transfer matrix method, has been widely used as a simple but intuitive model for micro-cavity effects in OLEDs [3]–[6]. In this analytical model, the light emission characteristic is described by two interference terms. The first is the multiple-beam interference (MBI) term, which results from the multiple resonances inside the OLED cavity and is described by the Fabry–Pérot resonator theory [17], [18]. The second corresponds to the two-beam interference (TBI) term, which describes the interference effect of the emission source itself [19]–[21]. However, the currently used Fabry–Pérot formulation has not yet included the effect of the dipole orientation and polarization dependency on the optical modeling of OLEDs. Moreover, all the Fabry–Pérot formulations for OLEDs had been adopted from the Fabry–Pérot formulations used for semiconductor LEDs [22], [23]. There is no research effort to demonstrate whether the Fabry–Pérot model for OLEDs is physically equivalent to the quantum-mechanical or the rigorous electromagnetic models. Thus, the validity and the limitation of the Fabry–Pérot formulation for OLEDs have yet to be investigated.

In this paper, we propose a generalized Fabry–Pérot formulation to consider the dipole orientation and polarization dependency in the optical modeling of OLEDs. The generalized Fabry–Pérot formulation is derived from the source-term method and becomes equivalent to the currently used Fabry–Pérot formulation in isotropic dipole orientation. The physical interpretation of the generalized Fabry–Pérot formulation is performed based on Fermi's golden rule. To demonstrate the applicability and the validity of the proposed optical modeling method, we calculate the angular emission characteristics of a top-emitting OLED with respect to the horizontal dipole ratio and the light polarization. The calculation results obtained by the generalized Fabry–Pérot formulation based on a simple analytical equation are matched with previous calculation results obtained by other modeling methods with mathematical and computational complexity.

2. Theory

2.1. Determination of the Electric Field Amplitudes

Typical OLEDs comprise a stack of thin-film multilayers, which are assumed to be isotropic and homogeneous with plane parallel interfaces. Fig. 1 shows a schematic diagram of OLEDs with forward- and backward-propagating electric field amplitude (E) in the coherent multilayer designated as the +(−) superscripts. We assume that each layer $w(w = 1, 2, \ldots, n)$ has a thickness of d_w and a complex refractive index of $\tilde{n}_w = n_w + i\kappa_w$, where n_w and κ_w are the refractive index and the extinction coefficient, respectively. The layer j is designated to be the emission layer with the thickness of $d_j = Z$, which is sandwiched between two coherent multilayers. In realistic working conditions of OLEDs, the emission layer is speculated to have a complex refractive index because the absorption or emission spectrum of the dipole emitter, which contributes to the imaginary part
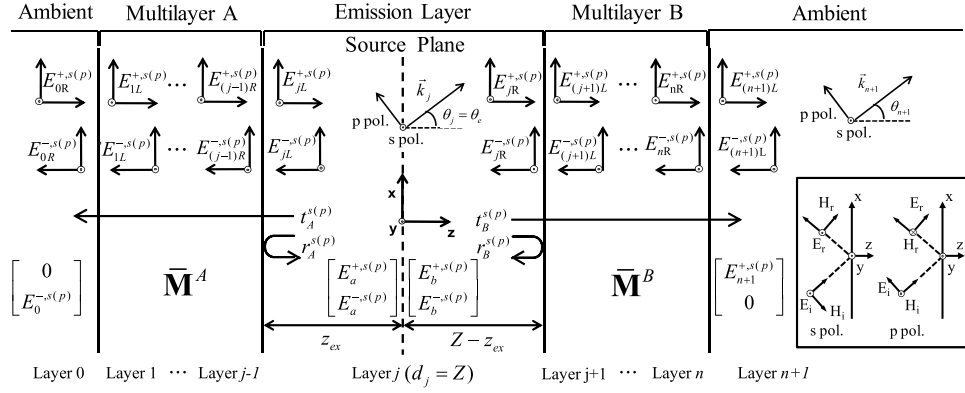
Fig. 1. Schematic diagram of OLEDs comprising coherent multilayers between semi-infinite transparent ambient. The forward- and backward-propagating electric field amplitudes (E) are designated as the +(−) superscripts, while s and p polarizations are denoted as the $s(p)$ superscripts. The layer j is designated to be the non-absorbing emission layer with the source plane. The sign convention for polarization-dependent reflection coefficients are shown in the inset.

of the complex refractive index, is matched with the operating wavelength. For simplicity, the emission layer is assumed to be non-absorbing in this derivation in accordance with other rigorous electromagnetic models for OLEDs [13]–[16]. Inside the emission layer, we assume that emission sources are confined to be at one interface. This is denoted as the source plane, which is z_{ex} distant from the left boundary of the emission layer. Light emission from the source plane is described by the wave vector of $\vec{k}_j$ and the emission angle of $\theta_j = \theta_e$, both of which are real in the non-absorbing emission layer. In the electric field amplitude, s and p polarizations are denoted as the $s(p)$ superscripts. The light emission is assumed to be extracted into the semi-infinite transparent ambient layer on the left ($w = 0$) and on the right ($w = n + 1$), which has only one electric-field component of $E_0^{-,s(p)}(w = 0)$ or $E_{n+1}^{+,s(p)}(w = n + 1)$. The extraction angle in the non-absorbing ambient layer is given by $n_j\sin\theta_j = n_{0(n+1)}\sin\theta_{0(n+1)}$ due to Snell's law of refraction [2], [14].

According to the transfer matrix method, the light propagation in the multilayer is described by means of the interface matrix ($\bar{\mathbf{I}}$) and the layer matrix ($\bar{\mathbf{L}}$) [24], [25]. The electric amplitudes at the interface between w-th and $(w + 1)$-th layer are written as

$$\begin{bmatrix} E_{wR}^{+,s(p)} \\ E_{wR}^{-,s(p)} \end{bmatrix} = \bar{\mathbf{I}}^{w/(w+1)} \begin{bmatrix} E_{(w+1)L}^{+,s(p)} \\ E_{(w+1)L}^{-,s(p)} \end{bmatrix} = \frac{1}{t_{w(w+1)}^{s(p)}} \begin{bmatrix} 1 & r_{w(w+1)}^{s(p)} \\ r_{w(w+1)}^{s(p)} & 1 \end{bmatrix} \begin{bmatrix} E_{(w+1)L}^{+,s(p)} \\ E_{(w+1)L}^{-,s(p)} \end{bmatrix} \tag{1}$$

where the subscript L and R represent the left and right boundaries of each layer. The terms $r_{w(w+1)}^{s(p)}$ and $t_{w(w+1)}^{s(p)}$ indicate the complex Fresnel reflection and transmission coefficients at the interface from the w-th to $(w + 1)$-th layer and are given by [25]

$$r_{w(w+1)}^s = \frac{\tilde{n}_w\cos\theta_w - \tilde{n}_{(w+1)}\cos\theta_{(w+1)}}{\tilde{n}_w\cos\theta_w + \tilde{n}_{(w+1)}\cos\theta_{(w+1)}} \tag{2}$$

$$r_{w(w+1)}^p = \frac{\tilde{n}_w\cos\theta_{(w+1)} - \tilde{n}_{(w+1)}\cos\theta_w}{\tilde{n}_w\cos\theta_{(w+1)} + \tilde{n}_{(w+1)}\cos\theta_w} \tag{3}$$

$$t_{w(w+1)}^s = \frac{2\tilde{n}_w\cos\theta_w}{\tilde{n}_w\cos\theta_w + \tilde{n}_{(w+1)}\cos\theta_{(w+1)}} \tag{4}$$

$$t_{w(w+1)}^p = \frac{2\tilde{n}_w\cos\theta_w}{\tilde{n}_w\cos\theta_{(w+1)} + \tilde{n}_{(w+1)}\cos\theta_w}. \tag{5}$$

Here, the sign convention for the polarization-dependent reflection coefficients is determined based on the inset of Fig. 1. The propagation of the electric field amplitude between the left and

right boundaries of the w-th layer is described by

$$\begin{bmatrix} E_{wR}^{+,s(p)} \\ E_{wR}^{-,s(p)} \end{bmatrix} = \bar{\mathbf{L}}^w(d_w) \begin{bmatrix} E_{wL}^{+,s(p)} \\ E_{wL}^{-,s(p)} \end{bmatrix} = \begin{bmatrix} e^{-ik_{z,w}d_w} & 0 \\ 0 & e^{ik_{z,w}d_w} \end{bmatrix} \begin{bmatrix} E_{wL}^{+,s(p)} \\ E_{wL}^{-,s(p)} \end{bmatrix} \tag{6}$$

where we assume the time dependence of $e^{i\omega t}$. The term $\tilde{k}_{z,w} = (2\pi/\lambda)\tilde{n}_w\cos\theta_w$ represents the z-component of the complex propagation constant in the w-th layer when λ is the wavelength of light in free space.

Source terms, being considered as oscillating dipole currents, are introduced as an additive discontinuity of the electromagnetic fields across the source plane [15]. The electric amplitude at the source plane is expressed as [16]

$$\begin{bmatrix} E_a^{+,s(p)} \\ E_a^{-,s(p)} \end{bmatrix} + \begin{bmatrix} A^{+,s(p)} \\ A^{-,s(p)} \end{bmatrix} = \begin{bmatrix} E_b^{+,s(p)} \\ E_b^{-,s(p)} \end{bmatrix} \tag{7}$$

where $E_a^{+(-),s(p)}$ and $E_b^{+(-),s(p)}$ are the values of the electric field amplitudes at the left and the right boundaries of the source plane, respectively. The source term $A^{+(-),s(p)}$ is given by the normalized power density of the dipole radiation, which will be shown later. When the transfer matrix method is applied, the terms $E_a^{+(-),s(p)}$ and $E_b^{+(-),s(p)}$ are related with the electric-field component in the ambient layer

$$\begin{bmatrix} 0 \\ E_0^{-,s(p)} \end{bmatrix} = \bar{\mathbf{M}}^A \bar{\mathbf{L}}^j(z_{ex}) \begin{bmatrix} E_a^{+,s(p)} \\ E_a^{-,s(p)} \end{bmatrix} = \begin{bmatrix} m_{11}^{A,s(p)} & m_{12}^{A,s(p)} \\ m_{21}^{A,s(p)} & m_{22}^{A,s(p)} \end{bmatrix} \begin{bmatrix} e^{-ik_{z,j}z_{ex}} & 0 \\ 0 & e^{ik_{z,j}z_{ex}} \end{bmatrix} \begin{bmatrix} E_a^{+,s(p)} \\ E_a^{-,s(p)} \end{bmatrix} \tag{8}$$

$$\begin{bmatrix} E_b^{+,s(p)} \\ E_b^{-,s(p)} \end{bmatrix} = \bar{\mathbf{L}}^j(Z-z_{ex})\bar{\mathbf{M}}^B \begin{bmatrix} E_{n+1}^{+,s(p)} \\ 0 \end{bmatrix} = \begin{bmatrix} e^{-ik_{z,j}(Z-z_{ex})} & 0 \\ 0 & e^{ik_{z,j}(Z-z_{ex})} \end{bmatrix} \begin{bmatrix} m_{11}^{B,s(p)} & m_{12}^{B,s(p)} \\ m_{21}^{B,s(p)} & m_{22}^{B,s(p)} \end{bmatrix} \begin{bmatrix} E_{n+1}^{+,s(p)} \\ 0 \end{bmatrix} \tag{9}$$

where the 2 × 2 system matrices on the left and right sides of the emission layer are $\bar{\mathbf{M}}^A = \bar{\mathbf{I}}^{0/1}\bar{\mathbf{L}}^1(d_1)\bar{\mathbf{I}}^{1/2},\ldots,\bar{\mathbf{L}}^{(j-1)}(d_{j-1})\bar{\mathbf{I}}^{(j-1)/j}$ and $\bar{\mathbf{M}}^B = \bar{\mathbf{I}}^{j/(j+1)}\bar{\mathbf{L}}^{j+1}(d_{j+1})\bar{\mathbf{I}}^{(j+1)/(j+2)},\ldots,\bar{\mathbf{L}}^n(d_n)\bar{\mathbf{I}}^{n/(n+1)}$. Equation (8) and (9) are mathematically equal to those in the source-term method [15], [16] except that the layer matrixes for the emission layer—$\bar{\mathbf{L}}^j(z_{ex}), \bar{\mathbf{L}}^j(Z-z_{ex})$—are separated from the 2 × 2 system matrices on the left and right sides of the emission layer. Further development of the analytical expressions of (8) and (9) will lead to a compact analytical equation of the proposed generalized Fabry–Pérot formulation as follows.

In Fig. 1, $r_A^{s(p)}$ and $t_A^{s(p)}$ represent the back-reflection and back-transmission coefficients from the layer j to 0. When the system matrix $\bar{\mathbf{M}}^A$ is used, they are expressed as [25]

$$r_A^{s(p)} = -r_{j/0}^{s(p)} = -\frac{m_{12}^{A,s(p)}}{m_{11}^{A,s(p)}} \tag{10}$$

$$t_A^{s(p)} = t_{j/0}^{s(p)} = \frac{m_{11}^{A,s(p)}m_{22}^{A,s(p)} - m_{12}^{A,s(p)}m_{21}^{A,s(p)}}{m_{11}^{A,s(p)}}. \tag{11}$$

In the same manner, $r_B^{s(p)}$ and $t_B^{s(p)}$ represent the front-reflection and front-transmission coefficients from the layer j to n+1 and are given by [25]

$$r_B^{s(p)} = r_{j/(n+1)}^{s(p)} = \frac{m_{21}^{B,s(p)}}{m_{11}^{B,s(p)}} \tag{12}$$

$$t_B^{s(p)} = t_{j/(n+1)}^{s(p)} = \frac{1}{m_{11}^{B,s(p)}}. \tag{13}$$

From (7) to (9), we obtain six simultaneous equations for six unknown variables of $E_a^{+,s(p)}$, $E_a^{-,s(p)}$ $E_b^{+,s(p)}$, $E_b^{-,s(p)}$, $E_0^{-,s(p)}$, and $E_{n+1}^{+,s(p)}$. After simple mathematical manipulation, we have

$$E_a^{+,s(p)} = \frac{-m_{12}^{A,s(p)} m_{21}^{B,s(p)} e^{ik_{z,j}Z} A^{+,s(p)} + m_{12}^{A,s(p)} m_{11}^{B,s(p)} e^{-ik_{z,j}Z} e^{i2k_{z,j}z_{ex}} A^{-,s(p)}}{m_{11}^{A,s(p)} m_{11}^{B,s(p)} e^{-ik_{z,j}Z} + m_{12}^{A,s(p)} m_{21}^{B,s(p)} e^{ik_{z,j}Z}} \tag{14}$$

$$E_a^{-,s(p)} = \frac{m_{11}^{A,s(p)} m_{21}^{B,s(p)} e^{ik_{z,j}Z} e^{-i2k_{z,j}z_{ex}} A^{+,s(p)} - m_{11}^{A,s(p)} m_{11}^{B,s(p)} e^{-ik_{z,j}Z} A^{-,s(p)}}{m_{11}^{A,s(p)} m_{11}^{B,s(p)} e^{-ik_{z,j}Z} + m_{12}^{A,s(p)} m_{21}^{B,s(p)} e^{ik_{z,j}Z}} \tag{15}$$

$$E_b^{+,s(p)} = \frac{m_{11}^{A,s(p)} m_{11}^{B,s(p)} e^{-ik_{z,j}Z} A^{+,s(p)} + m_{12}^{A,s(p)} m_{11}^{B,s(p)} e^{-ik_{z,j}Z} e^{i2k_{z,j}z_{ex}} A^{-,s(p)}}{m_{11}^{A,s(p)} m_{11}^{B,s(p)} e^{-ik_{z,j}Z} + m_{12}^{A,s(p)} m_{21}^{B,s(p)} e^{ik_{z,j}Z}} \tag{16}$$

$$E_b^{+,s(p)} = \frac{m_{11}^{A,s(p)} m_{11}^{B,s(p)} e^{-ik_{z,j}Z} A^{+,s(p)} + m_{12}^{A,s(p)} m_{11}^{B,s(p)} e^{-ik_{z,j}Z} e^{i2k_{z,j}z_{ex}} A^{-,s(p)}}{m_{11}^{A,s(p)} m_{11}^{B,s(p)} e^{-ik_{z,j}Z} + m_{12}^{A,s(p)} m_{21}^{B,s(p)} e^{ik_{z,j}Z}} \tag{17}$$

$$E_0^{-,s(p)} = \frac{\left(m_{11}^{A,s(p)} m_{22}^{A,s(p)} - m_{12}^{A,s(p)} m_{21}^{A,s(p)} \right) \left(m_{21}^{B,s(p)} e^{ik_{z,j}(Z-z_{ex})} A^{+,s(p)} - m_{11}^{B,s(p)} e^{-ik_{z,j}(Z-z_{ex})} A^{-,s(p)} \right)}{m_{11}^{A,s(p)} m_{11}^{B,s(p)} e^{-ik_{z,j}Z} + m_{12}^{A,s(p)} m_{21}^{B,s(p)} e^{ik_{z,j}Z}} \tag{18}$$

$$E_{n+1}^{+,s(p)} = \frac{m_{11}^{A,s(p)} e^{-ik_{z,j}z_{ex}} A^{+,s(p)} + m_{12}^{A,s(p)} e^{ik_{z,j}z_{ex}} A^{-,s(p)}}{m_{11}^{A,s(p)} m_{11}^{B,s(p)} e^{-ik_{z,j}Z} + m_{12}^{A,s(p)} m_{21}^{B,s(p)} e^{ik_{z,j}Z}}. \tag{19}$$

We will focus on the electric field amplitudes of $E_0^{-,s(p)}$ and $E_{n+1}^{+,s(p)}$, which describe the output light emission characteristics in the semi-infinite transparent ambient layer. When the definitions of the reflection and transmission coefficients from (10) to (13) are used, (18) and (19) can be expressed as

$$E_0^{-,s(p)} = \frac{\frac{m_{11}^{A,s(p)} m_{22}^{A,s(p)} - m_{12}^{A,s(p)} m_{21}^{A,s(p)}}{m_{11}^{A,s(p)}} \left(\frac{m_{21}^{B,s(p)}}{m_{11}^{B,s(p)}} e^{i2k_{z,j}Z} e^{-ik_{z,j}z_{ex}} A^{+,s(p)} - \frac{m_{11}^{B,s(p)}}{m_{11}^{B,s(p)}} e^{ik_{z,j}z_{ex}} A^{-,s(p)} \right)}{1 + \frac{m_{12}^{A,s(p)} m_{21}^{B,s(p)}}{m_{11}^{A,s(p)} m_{11}^{B,s(p)}} e^{i2k_{z,j}Z}}$$

$$= \frac{t_A^{s(p)} \left(r_B^{s(p)} e^{i2k_{z,j}Z} e^{-ik_{z,j}z_{ex}} A^{+,s(p)} - e^{ik_{z,j}z_{ex}} A^{-,s(p)} \right)}{1 - r_A^{s(p)} r_B^{s(p)} e^{i2k_{z,j}Z}} \tag{20}$$

$$E_{n+1}^{+,s(p)} = \frac{\frac{1}{m_{11}^{B,s(p)}} e^{ik_{z,j}Z} \left(e^{-ik_{z,j}z_{ex}} A^{+,s(p)} + \frac{m_{12}^{A,s(p)}}{m_{11}^{A,s(p)}} e^{ik_{z,j}z_{ex}} A^{-,s(p)} \right)}{1 + \frac{m_{12}^{A,s(p)} m_{21}^{B,s(p)}}{m_{11}^{A,s(p)} m_{11}^{B,s(p)}} e^{i2k_{z,j}Z}}$$

$$= \frac{t_B^{s(p)} e^{ik_{z,j}Z} \left(e^{-ik_{z,j}z_{ex}} A^{+,s(p)} - r_A^{s(p)} e^{ik_{z,j}z_{ex}} A^{-,s(p)} \right)}{1 - r_A^{s(p)} r_A^{s(p)} e^{i2k_{z,j}Z}}. \tag{21}$$

In (20) and (21), the common denominator corresponds to the MBI effect, which is also called the cavity quality factor Q. The different nominators are related with the TBI effect, which represents the interference between directly emitting and reflected radiation of a dipole emitter [19]–[21].

2.2. Determination of the Electric Field Intensities in the Outer Ambient Layer

The spontaneous emission of an OLED can be modeled by the Hertz dipole radiation with horizontal and vertical orientations. In the rigorous electromagnetic model, the spatial distribution of the dipole radiation in both near- and far-field zone is represented by a superposition of s- and p-polarized plane and evanescent waves, which corresponds to the Fourier transform over a different in-plane wave vector [13], [14]. The radiation pattern inside the multilayer structure of OLEDs can be obtained by taking proper plane wave components of the dipole radiation

pattern, which propagate and reach the multilayer structure. Thus, we can use the transfer matrix method to describe the electric field distribution in the multilayer structure if the source term, the plane wave component of the dipole radiation pattern, is given. When horizontal and vertical orientations of dipoles are denoted as the $h(v)$ subscripts, the radiation pattern of the Hertz dipole emitter can be described by the normalized spectral power density [15], [16]

$$P_h^s = \frac{3}{16\pi} \tag{22}$$

$$P_v^s = 0 \tag{23}$$

$$P_h^p = \frac{3}{16\pi}\cos^2\theta_e \tag{24}$$

$$P_v^p = \frac{3}{8\pi}\sin^2\theta_e \tag{25}$$

where θ_e is the emission angle in the emission layer in Fig. 1. The normalized spectral power density $P_{h(v)}^{s(p)}$ is assumed to be dimensionless. Thus, the source term $A^{+(-),s(p)}$ depends on the light polarization, the dipole orientation, and the emission angle, which is written as [15], [16]

$$A^{+,s(p)} = \sqrt{P_{h(v)}^{s(p)}}E_e^{+,s(p)} \tag{26}$$

$$A^{-,s(p)} = -\sqrt{P_{h(v)}^{s(p)}}E_e^{-,s(p)}. \tag{27}$$

Here, $E_e^{+,s(p)}$ and $E_e^{-,s(p)}$ are the forward- and backward-propagating electric field amplitudes at the source plane for s(p) polarizations, which will be cancelled out in (42) shown below. Substitution of (26) and (27) into (20) and (21) leads to

$$E_0^{-,s(p)} = \frac{t_A^{s(p)}\left(r_B^{s(p)}e^{i2k_{z,j}Z}e^{-ik_{z,j}z_{ex}} + e^{ik_{z,j}z_{ex}}\right)}{1 - r_A^{s(p)}r_B^{s(p)}e^{i2k_{z,j}Z}}\sqrt{P_{h(v)}^{s(p)}}E_e^{-,s(p)} \tag{28}$$

$$E_{n+1}^{+,s(p)} = \frac{t_B^{s(p)}e^{ik_{z,j}Z}\left(e^{-ik_{z,j}z_{ex}} + r_A^{s(p)}e^{ik_{z,j}z_{ex}}\right)}{1 - r_A^{s(p)}r_B^{s(p)}e^{i2k_{z,j}Z}}\sqrt{P_{h(v)}^{s(p)}}E_e^{+,s(p)}. \tag{29}$$

If the complex reflection coefficients are expressed as $r_A = |r_A|e^{-i\phi_A}$ and $r_B = |r_B|e^{-i\phi_B}$, the electric field intensity at the ambient layer on the left is written as

$$\begin{aligned}
\left|E_0^{-,s(p)}\right|^2 &= \frac{\left|t_A^{s(p)}\right|^2\left(r_B^{s(p)}e^{i2k_{z,j}Z}e^{-ik_{z,j}z_{ex}} + e^{ik_{z,j}z_{ex}}\right)\left(\left(r_B^{s(p)}\right)^*e^{-i2k_{z,j}Z}e^{+ik_{z,j}z_{ex}} + e^{-ik_{z,j}z_{ex}}\right)}{\left(1 - r_A^{s(p)}r_B^{s(p)}e^{i2k_{z,j}Z}\right)\left(1 - \left(r_A^{s(p)}\right)^*\left(r_B^{s(p)}\right)^*e^{-i2k_{z,j}Z}\right)}P_{h(v)}^{s(p)}\left|E_e^{-,s(p)}\right|^2 \\
&= \frac{\left|t_A^{s(p)}\right|^2\left[1 + \left|r_B^{s(p)}\right|^2 + \left|r_B^{s(p)}\right|e^{i\left[2k_{z,j}(Z-z_{ex})-\phi_B\right]} + \left|r_B^{s(p)}\right|e^{-i\left[2k_{z,j}(Z-z_{ex})-\phi_B\right]}\right]}{1 + \left|r_A^{s(p)}\right|^2\left|r_B^{s(p)}\right|^2 - \left|r_A^{s(p)}\right|\left|r_B^{s(p)}\right|e^{i(2k_{z,j}Z-\phi_A-\phi_B)} - \left|r_A^{s(p)}\right|\left|r_B^{s(p)}\right|e^{-i(2k_{z,j}Z-\phi_A-\phi_B)}}P_{h(v)}^{s(p)}\left|E_e^{-,s(p)}\right|^2.
\end{aligned} \tag{30}$$

The phase changes for the MBI can be defined as

$$\phi_{FP}^{s(p)} = 2k_{z,j}Z - \phi_A^{s(p)} - \phi_B^{s(p)} \tag{31}$$

where $\phi_{A(B)}^{s(p)}$ is the phase changes on reflection at the left (right) boundary of the emission layer. Similarly, the phase change for the TBI at the right boundary of the emission layer can be written as

$$\phi_{TB}^{B,s(p)} = 2k_{z,j}(Z - z_{ex}) - \phi_B^{s(p)}. \tag{32}$$

Thus, (30) can be expressed as

$$\left|E_0^{-,s(p)}\right|^2 = \frac{\left|t_A^{s(p)}\right|^2 \left(1 + \left|r_B^{s(p)}\right|^2 + 2\left|r_B^{s(p)}\right|\cos\phi_{TB}^{B,s(p)}\right)}{1 + \left|r_A^{s(p)}\right|^2\left|r_B^{s(p)}\right|^2 - 2\left|r_A^{s(p)}\right|\left|r_B^{s(p)}\right|\cos\phi_{FP}^{s(p)}} P_{h(v)}^{s(p)}\left|E_e^{-,s(p)}\right|^2. \tag{33}$$

If we set $R_{A(B)}^{s(p)} = \left|r_{A(B)}^{s(p)}\right|^2$ as the power reflectance at the left (right) boundary of the emission layer in Fig. 1, (33) can be written as

$$\left|E_0^{-,s(p)}\right|^2 = \frac{\left|t_A^{s(p)}\right|^2 \left(1 + R_B^{s(p)} + 2\sqrt{R_B^{s(p)}}\cos\phi_{TB}^{B,s(p)}\right)}{1 + R_A^{s(p)} R_B^{s(p)} - 2\sqrt{R_A^{s(p)}}\sqrt{R_B^{s(p)}}\cos\phi_{FP}^{s(p)}} P_{h(v)}^{s(p)}\left|E_e^{-,s(p)}\right|^2. \tag{34}$$

In the same manner, the electric field intensity at the ambient on the right can be simplified into

$$\left|E_{n+1}^{+,s(p)}\right|^2 = \frac{\left|t_B^{s(p)}\right|^2 \left(1 + R_A^{s(p)} + 2\sqrt{R_A^{s(p)}}\cos\phi_{TB}^{A,s(p)}\right)}{1 + R_A^{s(p)} R_B^{s(p)} - 2\sqrt{R_A^{s(p)}}\sqrt{R_B^{s(p)}}\cos\phi_{FP}^{s(p)}} P_{h(v)}^{s(p)}\left|E_e^{+,s(p)}\right|^2 \tag{35}$$

where the phase change for the TBI at the left boundary of the emission layer is defined as

$$\phi_{TB}^{A,s(p)} = 2k_{z,j}z_{ex} - \phi_A^{s(p)}. \tag{36}$$

It is noticeable that (34) can be easily obtained from (35) by replacing the TBI term at the left boundary of the emission layer with that at the right boundary of the emission layer and vice versa. In the case of double-emitting OLEDs [26], the output electric field intensities on both sides can be calculated based on (34) and (35). In general, the first layer ($w = 1$) in Fig. 1 comprises thick metal so that the electric field intensity on the left semi-infinite transparent ambient layer ($|E_0^{-,s(p)}|^2$) is zero. Thus, we will use only (35) for further derivation.

The degree of the dipole orientation can be expressed as [9]

$$P_{total}^{s(p)} = \Theta P_h^{s(p)} + (1 - \Theta)P_v^{s(p)} \tag{37}$$

where Θ represents the horizontal dipole ratio and has a value of 0.67 for completely isotropic dipole orientation. Referring to (22) and (23), (35) for s polarization is given by

$$\begin{aligned}
\left|E_{n+1}^{+,s}\right|^2 &= \frac{\left|t_B^s\right|^2 \left(1 + R_A^s + 2\sqrt{R_A^s}\cos\phi_{TB}^{A,s}\right)}{1 + R_A^s R_B^s - 2\sqrt{R_A^s}\sqrt{R_B^s}\cos\phi_{FP}^s} \left|E_e^{+,s}\right|^2 \left[\Theta P_h^s + (1 - \Theta)P_v^s\right] \\
&= \frac{\left|t_B^s\right|^2 \left(1 + R_A^s + 2\sqrt{R_A^s}\cos\phi_{TB}^{A,s}\right)}{1 + R_A^s R_B^s - 2\sqrt{R_A^s}\sqrt{R_B^s}\cos\phi_{FP}^s} \left|E_e^{+,s}\right|^2 \times \frac{3}{16\pi}\Theta.
\end{aligned} \tag{38}$$

Similarly, (35) for p polarization leads to

$$\begin{aligned}
\left|E_{n+1}^{+,p}\right|^2 &= \frac{\left|t_B^p\right|^2 \left(1 + R_A^p + 2\sqrt{R_A^p}\cos\phi_{TB}^{A,p}\right)}{1 + R_A^p R_B^p - 2\sqrt{R_A^p}\sqrt{R_B^p}\cos\phi_{FP}^p} \left|E_e^{+,p}\right|^2 \left[\Theta P_h^p + (1 - \Theta)P_v^p\right] \\
&= \frac{\left|t_B^p\right|^2 \left(1 + R_A^p + 2\sqrt{R_A^p}\cos\phi_{TB}^{A,p}\right)}{1 + R_A^p R_B^p - 2\sqrt{R_A^p}\sqrt{R_B^p}\cos\phi_{FP}^p} \left|E_e^{+,p}\right|^2 \left[\Theta \times \frac{3}{16\pi}\cos^2\theta_e + (1 - \Theta) \times \frac{3}{8\pi}\sin^2\theta_e\right].
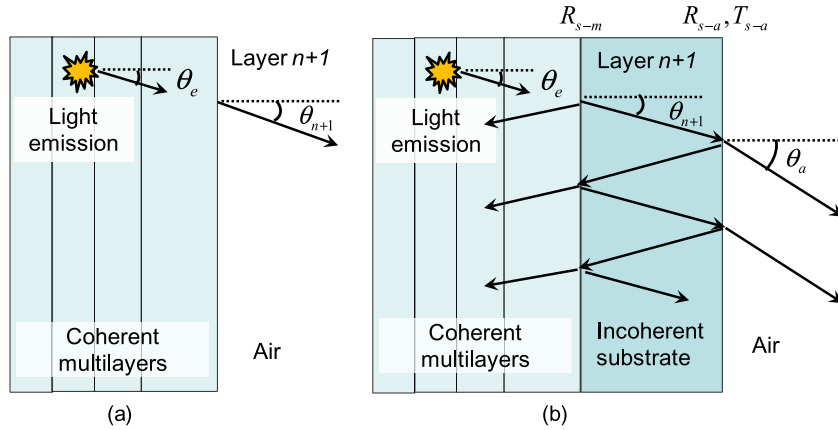\end{aligned} \tag{39}$$

Fig. 2. Schematic diagram of the light propagation from the emission layer to air. The outer transparent ambient layer (layer $n + 1$ in Fig. 1) is air for the top-emission OLED and the thick substrate for the bottom-emitting OLED. The angle in each layer is changed due to Snell's law of refraction. Because the thickness of the substrate (~1 mm) in the bottom-emitting OLED is much larger than the coherence length of the OLED light emission (~1 μm), the additional light propagation from the thick substrate to air should be treated as optically incoherent. The incoherent multiple reflections inside the thick substrate cause the reduction of the optical power extracted into air. (a) Top-emitting OLEDs. (b) Bottom-emitting OLEDs.

2.3. Derivation of a Generalized Fabry–Pérot Formulation

Fig. 2 shows a schematic diagram of the light propagation from the emission layer to air. The outer transparent ambient layer (layer $n + 1$ in Fig. 1) is air for the top-emission OLED and the thick substrate for the bottom-emitting OLED. The angle-dependent electroluminescent spectrum of OLEDs is proportional to the spectral radiant intensity [2], [27]. Because the thickness of the substrate (~1 mm) in the bottom-emitting OLED is much larger than the coherence length of the OLED light emission (~ 1 μm), the additional light propagation from the thick substrate to air should be treated as optically incoherent [28]–[31], which will be explained later. In calculating the spectral radiant intensity in the layer $n + 1$, we have to consider the fact that the projected area and the solid angle will change when the light propagates from the emission layer to the outer transparent ambient layer.

According to Snell's law of refraction, the angle in the emission layer (θ_e) is converted into the angle in the outer ambient layer (θ_{n+1}) by means of

$$n_e \sin\theta_e = n_{n+1} \sin\theta_{n+1} \tag{40}$$

where n_e and n_{n+1} are the real value of the refractive index in the emission layer and the layer $n + 1$. The change of the solid angle between the emission layer and the outer ambient layer is expressed as [15], [16]

$$\frac{d\Omega_e}{d\Omega_{n+1}} = \frac{\sin\theta_e \, d\theta_e}{\sin\theta_{n+1} \, d\theta_{n+1}} = \frac{n_{n+1}^2 \cos\theta_{n+1}}{n_e^2 \cos\theta_e}. \tag{41}$$

The optical power transmittance, which reflects the change of the projection area between the emission layer and the outer ambient layer, is given by [15], [16]

$$\frac{P_{n+1}^{s(p)}}{P_e^{s(p)}} = \frac{\vec{S}_{n+1}^{s(p)} \cdot \vec{A}_{n+1}}{\vec{S}_e^{s(p)} \cdot \vec{A}_e} = \frac{\frac{1}{2} c\varepsilon_0 n_{n+1} \left| E_{n+1}^{+,s(p)} \right|^2 \cos\theta_{n+1}}{\frac{1}{2} c\varepsilon_0 n_e \left| E_e^{+,s(p)} \right|^2 \cos\theta_e} = \frac{n_{n+1} \cos\theta_{n+1}}{n_e \cos\theta_e} \left| E_{n+1}^{+,s(p)} \right|^2 \tag{42}$$

where c is the speed of light in free space, and ε_0 is the electric permittivity in free space. The terms $\vec{S}_e^{s(p)}$ and $\vec{S}_{n+1}^{s(p)}$ represent the Poynting vector in the emission layer and the outer ambient

layer for $s(p)$ polarization. The unit normal vector to the surface is $\vec{A}_e$ and $\vec{A}_{n+1}$ for the emission layer and the outer layer, respectively. Finally, the output spectral radiant intensity [unit: W/(m$^2 \cdot$ sr $\cdot$ nm)] is written as

$$I_{R,n+1}^{s(p)}(\lambda,\theta_e) = \frac{dP_{n+1}^{s(p)}}{d\Omega_{n+1}dS} = \frac{dP_{n+1}^{s(p)}}{dP_e^{s(p)}}\frac{d\Omega_j}{d\Omega_{n+1}}\frac{dP_e^{s(p)}}{d\Omega_e dS} = \frac{n_{n+1}^3\cos^2\theta_{n+1}}{n_e^3\cos^2\theta_e}\left|E_{n+1}^{+,s(p)}\right|^2 I_{R,e}^{s(p)}(\lambda,\theta_e) \qquad (43)$$

where $I_{R,e}^{s(p)}(\lambda,\theta_e) = dP_e^{s(p)}/d\Omega_e dS$ is the spectral radiant intensity of the total dipole emitters under no micro-cavity effect. Experimentally, the photoluminescence spectrum can be used for $I_{R,e}^{s(p)}(\lambda,\theta_e)$ [16]. In theory, $I_{R,e}^{s(p)}(\lambda,\theta_e)$ can be calculated using several parameters such as a radiative efficiency, a normalized spectral density, and the ratio of the emitted photon energy to the injected elementary charge [2], [27].

Substitution of (38) and (39) into (43) leads to the output spectral radiant intensity for s and p polarizations as follows:

$$I_{R,n+1}^s(\lambda,\theta_{n+1}) = I_{R,e}^s(\lambda,\theta_e)\frac{n_{n+1}^3\cos^2\theta_{n+1}}{n_e^3\cos^2\theta_e}\frac{\left|t_B^s\right|^2\left(1+R_A^s+2\sqrt{R_A^s}\cos\phi_{TB}^{A,s}\right)}{1+R_A^s R_B^s - 2\sqrt{R_A^s}\sqrt{R_B^s}\cos\phi_{FP}^s}\frac{3}{16\pi}\Theta$$

$$= I_{R,e}^s(\lambda,\theta_e)\frac{T_B^s\left(1+R_A^{s(p)}+2\sqrt{R_A^{s(p)}}\cos\phi_{TB}^{A,s(p)}\right)}{1+R_A^{s(p)}R_B^{s(p)}-2\sqrt{R_A^{s(p)}}\sqrt{R_B^{s(p)}}\cos\phi_{FP}^{s(p)}}\frac{n_{n+1}^2\cos\theta_{n+1}}{n_e^2\cos\theta_e}\frac{3}{16\pi}\Theta. \qquad (44)$$

$$I_{R,n+1}^p(\lambda,\theta_{n+1}) = I_{R,e}^p(\lambda,\theta_e)\frac{n_{n+1}^3\cos^2\theta_{n+1}}{n_e^3\cos^2\theta_e}\frac{\left|t_B^p\right|^2\left(1+R_A^p+2\sqrt{R_A^p}\cos\phi_{TB}^{A,p}\right)}{1+R_A^p R_B^p - 2\sqrt{R_A^p}\sqrt{R_B^p}\cos\phi_{FP}^p}$$

$$\times\left[\Theta\frac{3}{16\pi}\cos^2\theta_e + (1-\Theta)\frac{3}{8\pi}\sin^2\theta_e\right]$$

$$= I_{R,e}^p(\lambda,\theta_e)\frac{T_B^p\left(1+R_A^p+2\sqrt{R_A^p}\cos\phi_{TB}^{A,p}\right)}{1+R_A^p R_B^p - 2\sqrt{R_A^p}\sqrt{R_B^p}\cos\phi_{FP}^p}\frac{n_{n+1}^2\cos\theta_{n+1}}{n_e^2\cos\theta_e}$$

$$\times\left[\Theta\frac{3}{16\pi}\cos^2\theta_e + (1-\Theta)\frac{3}{8\pi}\sin^2\theta_e\right]. \qquad (45)$$

Here, $T_B^{s(p)}$ indicates the power transmittance from the emission layer to the outer ambient layer on the right-hand side and is defined as

$$T_B^{s(p)} = \frac{n_{n+1}\cos\theta_{n+1}}{n_e\cos\theta_e}\left|t_B^{s(p)}\right|^2. \qquad (46)$$

Finally, the total output spectral radiant intensity is obtained by summing (44) and (45)

$$I_{R,n+1}(\lambda,\theta_{n+1},\Theta) = I_{R,e}^s(\lambda,\theta_e)\frac{T_B^s\left(1+R_A^s+2\sqrt{R_A^s}\cos\phi_{TB}^{A,s}\right)}{1+R_A^s R_B^s - 2\sqrt{R_A^s}\sqrt{R_B^s}\cos\phi_{FP}^s}\frac{n_{n+1}^2\cos\theta_{n+1}}{n_e^2\cos\theta_e}\frac{3}{16\pi}\Theta$$

$$+ I_{R,e}^p(\lambda,\theta_e)\frac{T_B^p\left(1+R_A^p+2\sqrt{R_A^p}\cos\phi_{TB}^{A,p}\right)}{1+R_A^p R_B^p - 2\sqrt{R_A^p}\sqrt{R_B^p}\cos\phi_{FP}^p}\frac{n_{n+1}^2\cos\theta_{n+1}}{n_e^2\cos\theta_e}\left[\Theta\frac{3}{16\pi}\cos^2\theta_e + (1-\Theta)\frac{3}{8\pi}\sin^2\theta_e\right] \qquad (47)$$

where $\theta_e = \sin^{-1}[(n_{n+1}/n_e)\sin\theta_{n+1}]$. Equation (47) is a generalized expression of the Fabry–Pérot formulation to calculate the dependence of the emission wavelength, the viewing angle, the dipole orientation ratio, and light polarization on the output emission characteristics of OLEDs.

This analytical expression is mathematically equivalent to the matrix-based numerical source-term method [15], [16] is much simpler than the rigorous electromagnetic model [13], [14].

If we take out the spectral radiant intensity of the total dipole emitters $I_{R,e}^{s(p)}(\lambda, \theta_e)$ in (47), we obtain the cavity enhancement factor $G_{R,n+1}(\lambda, \theta_{n+1}, \Theta)$ [5], [20], which is expressed as

$$G_{R,n+1}(\lambda, \theta_{n+1}, \Theta) = \frac{T_B^s\left(1 + R_A^s + 2\sqrt{R_A^s}\cos\phi_{TB}^{A,s}\right)}{1 + R_A^s R_B^s - 2\sqrt{R_A^s}\sqrt{R_B^s}\cos\phi_{FP}^s} \frac{n_{n+1}^2 \cos\theta_{n+1}}{n_e^2 \cos\theta_e} \frac{3}{16\pi}\Theta$$

$$+ \frac{T_B^p\left(1 + R_A^p + 2\sqrt{R_A^p}\cos\phi_{TB}^{A,p}\right)}{1 + R_A^p R_B^p - 2\sqrt{R_A^p}\sqrt{R_B^p}\cos\phi_{FP}^p} \frac{n_{n+1}^2 \cos\theta_{n+1}}{n_e^2 \cos\theta_e}\left[\Theta\frac{3}{16\pi}\cos^2\theta_e + (1-\Theta)\frac{3}{8\pi}\sin^2\theta_e\right]. \quad (48)$$

In the case of the isotropic dipole orientation ($\Theta_{iso} = 0.67$), (48) can be simplified into

$$G_{R,n+1}(\lambda, \theta_{n+1}, \Theta_{iso})$$

$$= \left[\frac{T_B^s\left(1 + R_A^s + 2\sqrt{R_A^s}\cos\phi_{TB}^{B,s}\right)}{1 + R_A^s R_B^s - 2\sqrt{R_A^s}\sqrt{R_B^s}\cos\phi_{FP}^s} + \frac{T_B^p\left(1 + R_A^p + 2\sqrt{R_A^p}\cos\phi_{TB}^{B,p}\right)}{1 + R_A^p R_B^p - 2\sqrt{R_A^p}\sqrt{R_B^p}\cos\phi_{FP}^p}\right] \frac{n_{n+1}^2 \cos\theta_{n+1}}{n_e^2 \cos\theta_e} \frac{1}{8\pi}. \quad (49)$$

In this case, the angular dependence of the source term disappears. The angular dependence of the cavity enhancement factor takes place at the transmittance and reflectance of the multilayer together with the phase change on reflection. Furthermore, in normal emission ($\theta_{n+1} = 0°$), (49) is further reduced to

$$G_{R,n+1}(\lambda, \theta_{n+1} = 0°, \Theta_{iso}) = \frac{T_B\left(1 + R_A + 2\sqrt{R_A}\cos\phi_{TB}^B\right)}{1 + R_A R_B - 2\sqrt{R_A}\sqrt{R_B}\cos\phi_{FP}} \frac{n_{n+1}^2}{n_e^2} \frac{1}{4\pi} \quad (50)$$

where we have the relations of $T_B = T_B^s = T_B^p$, $R_{A(B)} = R_{A(B)}^s = R_{A(B)}^p$, $\phi_{FP} = \phi_{FP}^s = \phi_{FP}^p$, and $\phi_{TB}^B = \phi_{TB}^{B,s} = \phi_{TB}^{B,p}$ due to the degeneracy of s and p polarizations in normal emission. We can easily show that (50) can be converted into the previous Fabry–Pérot formulations in the literature as follows [1], [18], [19]:

$$G_{R,n+1}(\lambda, \theta_{n+1} = 0°, \Theta_{iso}) = \frac{T_B\left[(1 + \sqrt{R_A})^2 - 2\sqrt{R_A}\left(1 - \cos\phi_{TB}^B\right)\right]}{(1 - \sqrt{R_A}\sqrt{R_B})^2 + 2\sqrt{R_A}\sqrt{R_B}(1 - \cos\phi_{FP})} \times \frac{n_{n+1}^2}{n_e^2}\frac{1}{4\pi} \quad (51)$$

$$= \frac{T_B\left(1 + R_A + 2\sqrt{R_A}\cos\phi_{TB}^B\right)}{(1 - \sqrt{R_A}\sqrt{R_B})^2 + 4\sqrt{R_A}\sqrt{R_B}\sin^2\frac{\phi_{FP}}{2}} \times \frac{n_{n+1}^2}{n_e^2}\frac{1}{4\pi} \quad (52)$$

$$= \frac{T_B(1 + \sqrt{R_A})^2\left[1 - \frac{4\sqrt{R_A}}{(1+\sqrt{R_A})^2}\sin^2\frac{\phi_{TB}^B}{2}\right]}{(1 - \sqrt{R_A}\sqrt{R_B})^2 + 4\sqrt{R_A}\sqrt{R_B}\sin^2\frac{\phi_{FP}}{2}} \times \frac{n_{n+1}^2}{n_e^2}\frac{1}{4\pi} \quad (53)$$

where the value of $1/4\pi$. indicates a solid angle for the dipole emitter because the spontaneous emission of an OLED is described by the normalized spectral power density. The term n_{n+1}^2/n_e^2 originates from the change in the solid angle between the emission layer and the outer ambient layer.

In Fig. 2(b), the outer layer $n + 1$ in the bottom-emitting OLED corresponds to the thick substrate, which should be treated as optically incoherent because its thickness (~1 mm) is much larger than the coherence length of the OLED light emission [28]–[31]. Because the thick substrate is incoherent, the change in the substrate thickness will not cause the interference effect within the coherent multilayer and not affect the electric field intensities in (34) and (35). Instead, the incoherent multiple reflections inside the thick substrate cause the reduction of the optical

power extracted into air, as shown in Fig. 2(b). The fraction of incoherent power transmission from the incoherent substrate to air is given by [30]

$$T_{\text{sub}}^{s(p)} = \frac{T_{s-a}^{s(p)}}{1 - R_{s-a}^{s(p)} R_{s-m}^{s(p)}} \tag{54}$$

where T_{s-a} and R_{s-a} is the transmittance and reflectance from the substrate to air, respectively. The term is R_{s-m} is the reflectance from the substrate to the coherent multilayer [30]. In addition, we should consider the variation of the solid angle when the light propagates from the thick substrate to air. When Snell's law of refraction is applied, the conversion of the angle in the substrate (θ_{n+1}) into the angle in the air (θ_a) leads to

$$n_e \sin\theta_e = n_{n+1} \sin\theta_{n+1} = n_a \sin\theta_a \tag{55}$$

where $n_a = 1$ is the refractive index of air. Correspondingly, the change of the solid angle between the thick substrate and air is

$$\frac{d\Omega_{n+1}}{d\Omega_a} = \frac{\sin\theta_{n+1} d\theta_{n+1}}{\sin\theta_a d\theta_a} = \frac{n_a^2 \cos\theta_a}{n_{n+1}^2 \cos\theta_{n+1}}. \tag{56}$$

Finally, the cavity enhancement factor of the bottom-emitting OLED can be obtained by multiplying correction factors by (48), which is expressed as

$$
\begin{aligned}
G_{R,a}(\lambda, \theta_a, \Theta) =\ & \frac{T_{\text{sub}}^s T_B^s \left(1 + R_A^s + 2\sqrt{R_A^s}\cos\phi_{\text{TB}}^{A,s}\right)}{1 + R_A^s R_B^s - 2\sqrt{R_A^s}\sqrt{R_B^s}\cos\phi_{\text{FP}}^s} \frac{n_a^2 \cos\theta_a}{n_e^2 \cos\theta_e} \frac{3}{16\pi}\Theta \\
& + \frac{T_{\text{sub}}^p T_B^p \left(1 + R_A^p + 2\sqrt{R_A^p}\cos\phi_{\text{TB}}^{A,p}\right)}{1 + R_A^p R_B^p - 2\sqrt{R_A^p}\sqrt{R_B^p}\cos\phi_{\text{FP}}^p} \frac{n_a^2 \cos\theta_a}{n_e^2 \cos\theta_e} \left[\Theta \frac{3}{16\pi}\cos^2\theta_e + (1 - \Theta)\frac{3}{8\pi}\sin^2\theta_e\right].
\end{aligned} \tag{57}
$$

2.4. Application Scope of a Generalized Fabry–Pérot Formulation

The light coupling mechanism in a bottom-emitting OLED includes the radiation mode extracted into air, the substrate mode trapped in the thick substrate, the waveguide mode trapped in the multiple organic layers, and the evanescent surface plasmon mode generated at the metal-dielectric interface while the substrate mode is not existent in a top-emitting OLED [1], [2]. Quantifying all the light coupling mechanisms in bottom- or top-emitting OLEDs is necessary to optimize the light extraction methods or to evaluate the external quantum efficiency (EQE). For this purpose, the rigorous electromagnetic model such as the power spectrum method [2], [14] should be used in spite of its heavy mathematical and computational complexity.

The Fabry–Pérot formulation, including the proposed generalized Fabry–Pérot formulation, deals with only the radiation mode, which is a far-field plane wave extracted into air. In both top- and bottom-emitting OLEDs, the radiation mode is extracted from the emission layer into air with the emission angle of $0 \leq \theta_e \leq \sin^{-1}(1/n_e)$. It can be shown that the generalized Fabry–Pérot formulation can be mathematically equivalent to the radiation mode part of the power spectrum method. For convenience, we prove the equivalence for the s-polarized radiation mode emitted by the horizontally-oriented dipole, but other two cases can be also proven in the same manner. In the power spectrum method, the light coupling process is described by the normalized in-plane wave vector [2], [14]. According to [2, App.], the normalized power density per unit normalized in-plane wave vector for the s-polarized radiation mode emitted by the horizontally-oriented dipole $K'_{h,s}(u)$ is given by

$$K'_{h,s}(u) = \frac{3}{16} \frac{1}{\sqrt{1 - u^2}} \frac{\left|1 + a_s^-\right|^2}{\left|1 - a_s^+ a_s^-\right|^2} T_s^+ \tag{58}$$

where $u = \sin\theta_e$ is the normalized in-plane wave vector, and we have the relation of $a_s^+ = r_s^+ \exp(2ik_{z,j}z^+)$ and $a_s^- = r_s^- \exp(2ik_{z,j}z^-)$. The term $r_s^{+(-)}$ is the reflection coefficient in the forward- and backward-propagating direction. The term $z^{+(-)}$ is the distance of the dipole emitter from the right-hand (left-hand boundary) of the emission layer. In reference to Fig. 1, we have $a_s^+ = r_B^s \exp[2ik_{z,j}(Z - z_{ex})]$ and $a_s^- = r_A^s \exp(2ik_{z,j}z_{ex})$, respectively. Finally, the power transmittance for s polarization is written as

$$T_s^+ = \left|t_s^s\right|^2 \frac{k_{z,n+1}}{k_{z,j}} = \left|t_B^s\right|^2 \frac{n_{n+1}\cos\theta_{n+1}}{n_e\cos\theta_e} \qquad (59)$$

where $k_{z,j}$ and $k_{z,n+1}$ are the out-of-plane wave vectors in the emission layer and the outer ambient layer, respectively. In the case of the radiation mode, the normalized spectral power density per unit normalized in-plane wave vector $K'_{h,s}(u)$ can be converted into a spectral power density per unit solid angle $P'_{h,s}(\theta_{n+1})$, which is equivalent to the cavity enhancement factor $G_h^s(\theta_{n+1})$ [2], [14]

$$P'_{h,s}(\theta_{n+1}) = \left(\frac{n_{n+1}}{n_e}\right)^2 \frac{\cos\theta_{n+1}}{\pi} K'_{h,s}(\sin\theta_e). \qquad (60)$$

Substitution of (58) and (59) into (60) leads to

$$
\begin{aligned}
P'_{h,s}(\theta_{n+1}) &= \left(\frac{n_{n+1}}{n_e}\right)^2 \frac{\cos\theta_{n+1}}{\pi} \frac{3}{16} \frac{1}{\cos\theta_e} \left|\frac{1 + r_A^s e^{2ik_{z,j}z_{ex}}}{1 - r_A^s r_B^s e^{i2k_{z,j}Z}}\right|^2 \left|t_B^s\right|^2 \frac{n_{n+1}\cos\theta_{n+1}}{n_e\cos\theta_e} \\
&= \frac{n_{n+1}^3 \cos^2\theta_{n+1}}{n_e^3 \cos^2\theta_e} \frac{\left|t_B^s\right|^2 \left(1 + R_A^s + 2\sqrt{R_A^{\bar{s}}}\cos\phi_{TB}^{A,s}\right)}{1 + R_A^s R_B^s - 2\sqrt{R_A^{\bar{s}}}\sqrt{R_B^{\bar{s}}}\cos\phi_{FP}^s} \frac{3}{16\pi} \\
&= \frac{T_B^s\left(1 + R_A^s + 2\sqrt{R_A^{\bar{s}}}\cos\phi_{TB}^{A,s}\right)}{1 + R_A^s R_B^s - 2\sqrt{R_A^{\bar{s}}}\sqrt{R_B^{\bar{s}}}\cos\phi_{FP}^s} \frac{n_{n+1}^2 \cos\theta_{n+1}}{n_e^2 \cos\theta_e} \frac{3}{16\pi}.
\end{aligned}
\qquad (61)
$$

Equation (61) is the same as the first term of (48), except for the horizontal dipole ratio of Θ. Thus, the radiation mode part of the power spectrum method can be converted into the analytical expression of the generalized Fabry–Pérot formulation, which is much simpler and provides the better design guideline.

The proposed Fabry–Pérot formulation has a limitation in that it is not applicable to the calculation of the trapped optical coupling mechanisms such as the substrate mode, the waveguide mode, and the surface plasmon mode. In addition, the proposed Fabry–Pérot formulation cannot give a quantitatively absolute value of the EQE or the Purcell factor because all the light coupling mechanisms should be considered in these calculations. Although the application of the Fabry–Pérot formulation is only limited to the radiation mode, the Fabry–Pérot formulation is still a very useful and widely used modeling method to optimize the multilayer structure of OLEDs, where only the consideration of the radiation mode is sufficient to maximize the output intensity under the micro-cavity effect [3]–[6]. Thus, the generalized Fabry–Pérot formulation is more efficient than the rigorous electromagnetic model when we come to calculate the effect of the dipole orientation and light polarization on output characteristics of OLEDs, where only the radiation mode plays an important role.

3. Physical Interpretation Based on Fermi's Golden Rule

In the quantum-mechanical picture, spontaneous emission in organic electroluminescent media is described by coupling of an electrical dipole transition to photonic modes [2]. According to Fermi's golden rule in quantum electrodynamics, the optical transition rate (Γ) between the excited-energy state $|j\rangle$ and the lower-energy state $|i\rangle$ is given by [32]

$$\Gamma = \frac{2\pi}{\hbar}\rho(\nu)\left|\left\langle j\left|\vec{\mu}\cdot\vec{E}(\vec{r}_e)\right|i\right\rangle\right|^2 \qquad (62)$$
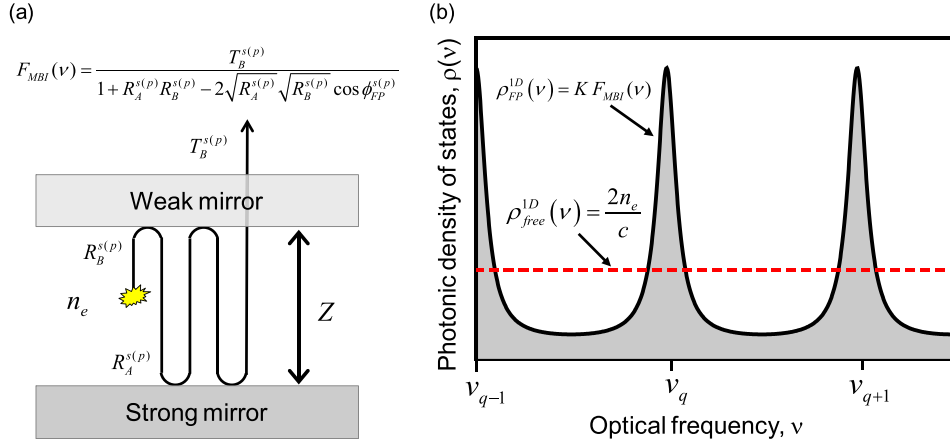
(a)

$$F_{MBI}(\nu) = \frac{T_B^{s(p)}}{1 + R_A^{s(p)} R_B^{s(p)} - 2\sqrt{R_A^{s(p)}}\sqrt{R_B^{s(p)}}\cos\phi_{FP}^{s(p)}}$$

$T_B^{s(p)}$

Weak mirror

$R_B^{s(p)}$

n_e

Z

$R_A^{s(p)}$

Strong mirror

(b)

Photonic density of states, $\rho(\nu)$

$\rho_{FP}^{1D}(\nu) = K\, F_{MBI}(\nu)$

$\rho_{free}^{1D}(\nu) = \dfrac{2n_e}{c}$

ν_{q-1} ν_q ν_{q+1}

Optical frequency, ν

Fig. 3. (a) Schematic diagram of the MBI term in the Fabry–Pérot formulation. The MBI term $F_{MBI}(\nu)$ is equal to the Airy's factor and represents the optical transmittance of the Fabry–Pérot resonator in a single direction. (n_e is the refractive index of the emission layer, and Z is the thickness of the emission layer.) (b) Schematic diagram of the photonic density of states in free space (red dashed line) and in the Fabry–Pérot resonator (solid line). The photonic density of states in the Fabry–Pérot resonator has a maximal value at the resonance frequencies of $\nu_{q-1}, \nu_q, \nu_{q+1}, \ldots$, where q is an integer. The photonic density of states inside the emission layer is redistributed due to the Fabry–Pérot interference, which is well described by the MBI term in the proposed Fabry–Pérot formulation.

where $\hbar$ is the Planck constant, and $\vec{\mu}$ is the electric dipole moment. The optical transition rate in the quantum-mechanical picture is determined by the following three factors. The photonic density of states $\rho(\nu)$ is the number of photonic modes per unit frequency interval at the emitter frequency ν. The term $\vec{E}(\vec{r_e})$ represents the amplitude of the electric field at the emitter position $(\vec{r_e})$. Finally, $\vec{\mu} \cdot \vec{E}$ corresponds to the orientation of the electric field with respect to the electric dipole direction.

The proposed Fabry–Pérot formulation for OLEDs includes all the factors used in the quantum-mechanical picture. For simplicity, we restrict our description to the normal dipole emission, which can be easily generalized for oblique dipole emission. Referring to Fig. 3(a), the MBI term in (47) is written as

$$F_{\text{MBI}}(\nu) = \frac{T_B^{s(p)}}{1 + R_A^{s(p)} R_B^{s(p)} - 2\sqrt{R_A^{s(p)}}\sqrt{R_B^{s(p)}}\cos\phi_{\text{FP}}^{s(p)}} \tag{63}$$

$$\phi_{\text{FP}}^{s(p)} = 4\pi n_e Z \nu / c - \phi_A^{s(p)} - \phi_B^{s(p)} \tag{64}$$

where ν is the frequency of light. The MBI term $F_{\text{MBI}}(\nu)$ is equal to the Airy's factor and corresponds to the optical transmittance of the Fabry–Pérot resonator in a single direction [33]. If a one-dimensional homogeneous medium of the emission layer is located in free space, the photonic density of vacuum states is given by [17]

$$\rho_{\text{free}}^{1D}(\nu) = \frac{2n_e}{c}. \tag{65}$$

The photonic density of states along the cavity axis is proportional to the optical transmittance through the cavity in a one-dimensional planar micro-cavity [34]. The photonic density of states in the emission layer is expressed as

$$\rho_{\text{FP}}^{1D}(\nu) = K\, F_{\text{MBI}}(\nu) \tag{66}$$

where the value of a constant K can be determined by the normalization condition of the photonic density of states [33]. As shown in Fig. 3(b), the photonic density of states is greatly
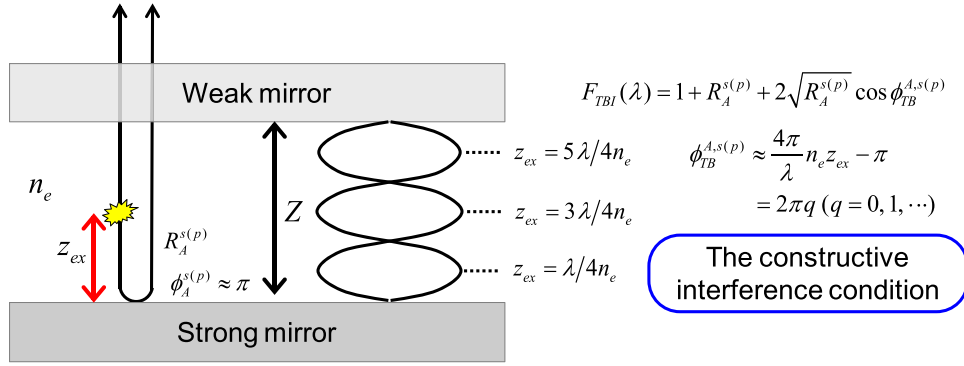
Fig. 4. (a) Schematic diagram of the TBI term $F_{TBI}(\lambda)$ in the Fabry–Pérot formulation. The optical reflection at the strong metal mirror gives an approximate phase shift of π. The TBI term is maximized at the constructive interference condition, which is satisfied at the dipole positions of $z_{ex} = \lambda/4n_e, 3\lambda/4n_e, 5\lambda/4n_e, \cdots$. These optimal dipole positions correspond to the antinode positions of the extracted electric field inside the cavity. The TBI term in the proposed Fabry–Pérot formulation represents the amplitude of the electric field at the emitter position in the quantum-mechanical picture.

modified from $\rho_{free}^{1D}(\nu)$ to $\rho_{FP}^{1D}(\nu)$ due to the Fabry–Pérot resonance in the emission layer. Thus, the MBI term in the proposed Fabry–Pérot formulation can properly describe the redistribution of the photonic density of vacuum states caused by the Fabry–Pérot interference.

As shown in Fig. 4, the TBI term in (47) is given by

$$F_{TBI}(\lambda) = 1 + R_A^{s(p)} + 2\sqrt{R_A^{s(p)}}\cos\phi_{TB}^{A,s(p)} \tag{67}$$

$$\phi_{TB}^{A,s(p)} = \frac{4\pi}{\lambda}n_e z_{ex} - \phi_A^{s(p)} \tag{68}$$

where z_{ex} is the distance of the dipole emitter from the strong mirror. Because optical reflection at the strong metal mirror approximately gives a phase shift of π, the phase change in (68) leads to

$$\phi_{TB}^{A,s(p)} \approx \frac{4\pi}{\lambda}n_e z_{ex} - \pi. \tag{69}$$

The TBI term $T_{TBI}(v)$ has a maximum value whenever $\phi_{TB}^{A,s(p)}$ satisfies the constructive interference condition. The optimal dipole positions to maximize the TBI tem are given by

$$z_{ex}^{max} = \frac{\lambda}{4n_e}, \frac{3\lambda}{4n_e}, \frac{5\lambda}{4n_e}, \ldots. \tag{70}$$

The amplitude of the electric field becomes approximately zero at the interface of the highly-absorbing strong mirror made of metal. Thus, the optimal dipole positions correspond to the antinode positions of the extracted electric field inside the cavity, as shown in Fig. 4. This is the reason why the TBI term in the proposed Fabry–Pérot formulation is called as the antinode factor [34], which represents the amplitude of the electric field at the emitter position in the quantum-mechanical picture. Finally, the normalized spectral power densities given in (22)–(25) describe the light emission depending on the electric dipole orientation with respect to the electric field direction, which corresponds to the term $\vec{\mu} \cdot \vec{E}$ in Fermi's golden rule of (62).

4. Application Example

To demonstrate the applicability and the validity of the generalized Fabry–Pérot formulation to the optical modeling of OLEDs, we obtain the calculation results in a simple application
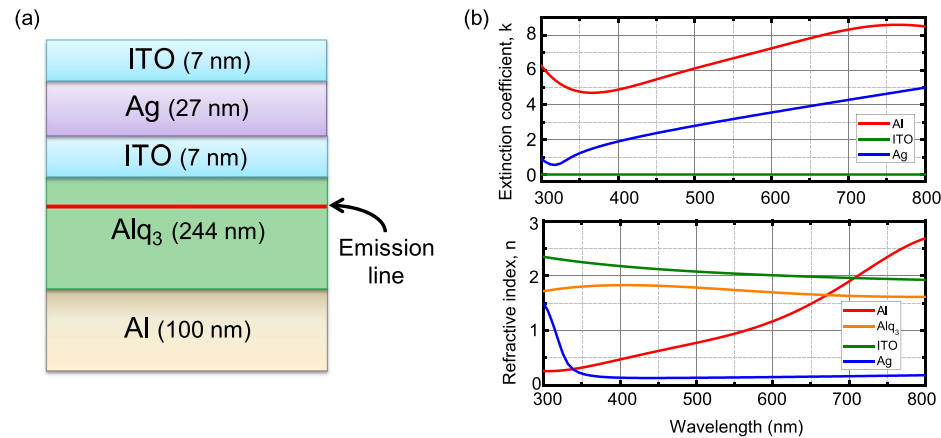
Fig. 5. (a) Device structure of a top-emitting OLED along with the corresponding layer thickness. The δ-distributed emission zone is marked as a red line. (b) Complex refractive index spectra of each layer.
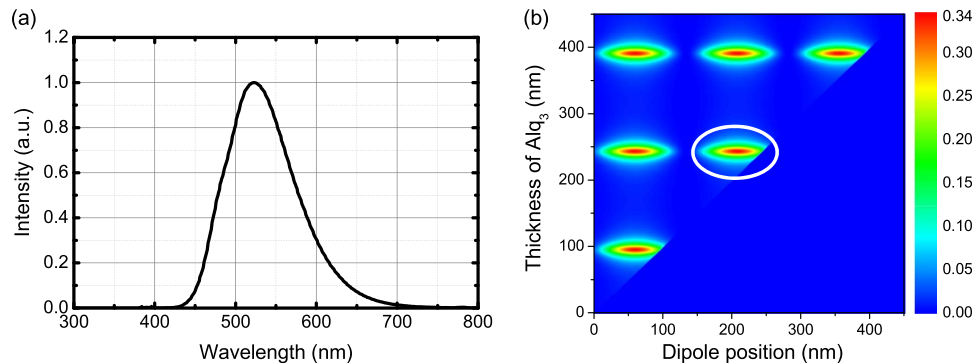

Fig. 6. (a) PL spectrum of the Alq$_3$ organic emission layer. (b) Two-dimensional Contour plot of the calculated total output intensity in normal direction as the thicknesses of the emission layer and the position of the dipole emitter are varied. The position of the dipole emitter is set to be 208 nm (marked as a white circle) from the reflective bottom anode, which corresponds to the second resonance condition at the emission-layer thickness of 244 nm.

example of the top-emitting OLED used in [35]. Using the simple analytical formula in (47), we calculate the dependence of the dipole orientation and light polarization on the output intensity and spectrum, which shows the same tendency as other optical modeling methods did [7]–[9]. Fig. 5(a) shows a device structure along with its layer thickness, which is composed of Al (aluminum) as a reflective bottom anode, Alq$_3$ (tris-(8-hydroxyquinoline)aluminum) as an organic emission layer, and indium-tin oxide (ITO)/Ag (silver)/ITO as a semi-transparent top cathode. For simplicity, we assume that both the carrier transport and the exciton generation take place at the Alq$_3$ layer. We further assume that the exciton generation region or emission region is infinitely thin and has a δ-function distribution, as denoted in Fig. 5(a). The complex refractive index spectra of each material are shown in Fig. 5(b). Complex refractive indices of materials, except Ag, are taken from the literatures [36], and that of Ag is obtained from the referenced web site [37]. In the Fabry–Pérot formulation, the refractive index of the emission layer is assumed to be real so that the extinction coefficient of Alq$_3$ is not considered in Fig. 5(b).

The photoluminescence (PL) spectrum of Alq$_3$ used for the organic emission layer is shown in Fig. 6(a). A green-emitting Alq$_3$ has the PL peak at the center wavelength of 520 nm. The organic emission layer of Alq$_3$ is speculated to have the isotropic dipole orientation ($\Theta = 0.67$) because the refractive index of Alq$_3$ is optically isotropic [38]. The exciton dipole position from the
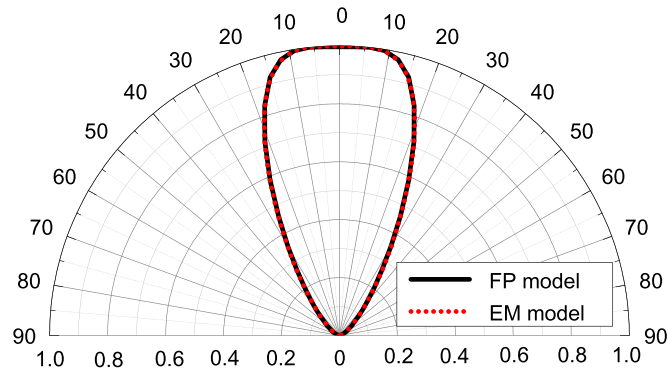
Fig. 7. Angular emission characteristics calculated by the generalized Fabry–Pérot formulation (black solid line) and the rigorous electromagnetic model (red dot line) at the same OLED structure of Fig. 6(a). The calculation is performed at the single wavelength of 520 nm. The light intensity is normalized in reference to the intensity at the viewing angle of 0°.

reflective bottom anode and the thickness of the Alq$_3$ emission layer are determined with the consideration of the micro-cavity effect. Fig. 6(b) shows the 2-D contour plot of the calculated total output radiant intensity as the thicknesses of the emission layer and the position of the exciton dipole emitter are varied. The thicknesses of the ITO/Ag/ITO semi-transparent top cathode are designed to maximize the total output radiant intensity in normal direction under the center wavelength of 520 nm when the dipole orientation is isotropic. The position of the dipole emitter is set to be 208 nm from the reflective bottom anode, which corresponds to the second resonance condition at the emission-layer thickness of 244 nm.

To verify the accuracy of the generalized Fabry–Pérot formulation, the output intensity is calculated at the same OLED structure of Fig. 5(a) compared with the rigorous electromagnetic model [14]. Fig. 7 shows the calculation results of angular emission characteristics at the wavelength of 520 nm, which corresponds to the peak wavelength of the PL spectrum in Fig. 6(a). The horizontal dipole ratio of Alq$_3$ is assumed to be 0.67, and the contribution of both s and p polarizations is added. The light intensity is normalized in reference to the intensity at the viewing angle of 0°. The two calculation results agree with each other, which demonstrate the accuracy of the generalized Fabry–Pérot formulation to the optical modeling for the top-emitting OLED.

Fig. 8 shows the 2-D contour plot of the angular emission spectra depending on the horizontal dipole ratio and light polarization. For convenience, we assume the horizontal dipole ratio of the Alq$_3$ layer to have a value of $\Theta = 0.57$, 0.67, and 0.77 although the actual dipole orientation of the Alq$_3$ layer is speculated to be isotropic ($\Theta = 0.67$). The vertically oriented dipoles have a little contribution on the extracted light, as shown in (23) and (25). As the horizontal dipole ratio increases, the overall angular emission spectra become enhanced at all the extraction angles and the light polarizations, which agree with the other calculation results in terms of the dipole orientation dependency [7]–[9].

Fig. 9 shows the calculation results of the total extraction intensity as a function of the extraction angle in various combinations of the horizontal dipole ratio and the light polarization. The total extraction intensity becomes larger at the higher horizontal dipole ratio and p-polarized light, which is matched with the previous calculation results based on other modeling methods of OLEDs [7]–[12]. It is obvious that both the dipole orientation and the light polarization play an important role in the output intensity of OLEDs, which can be easily calculated based on the proposed generalized Fabry–Pérot formulation.

5. Conclusion

We proposed a generalized Fabry–Pérot formulation in the optical modeling of OLEDs, which can easily calculate the effect of the dipole orientation and light polarization on the angular emission spectra without the use of complicated rigorous electromagnetic models. The
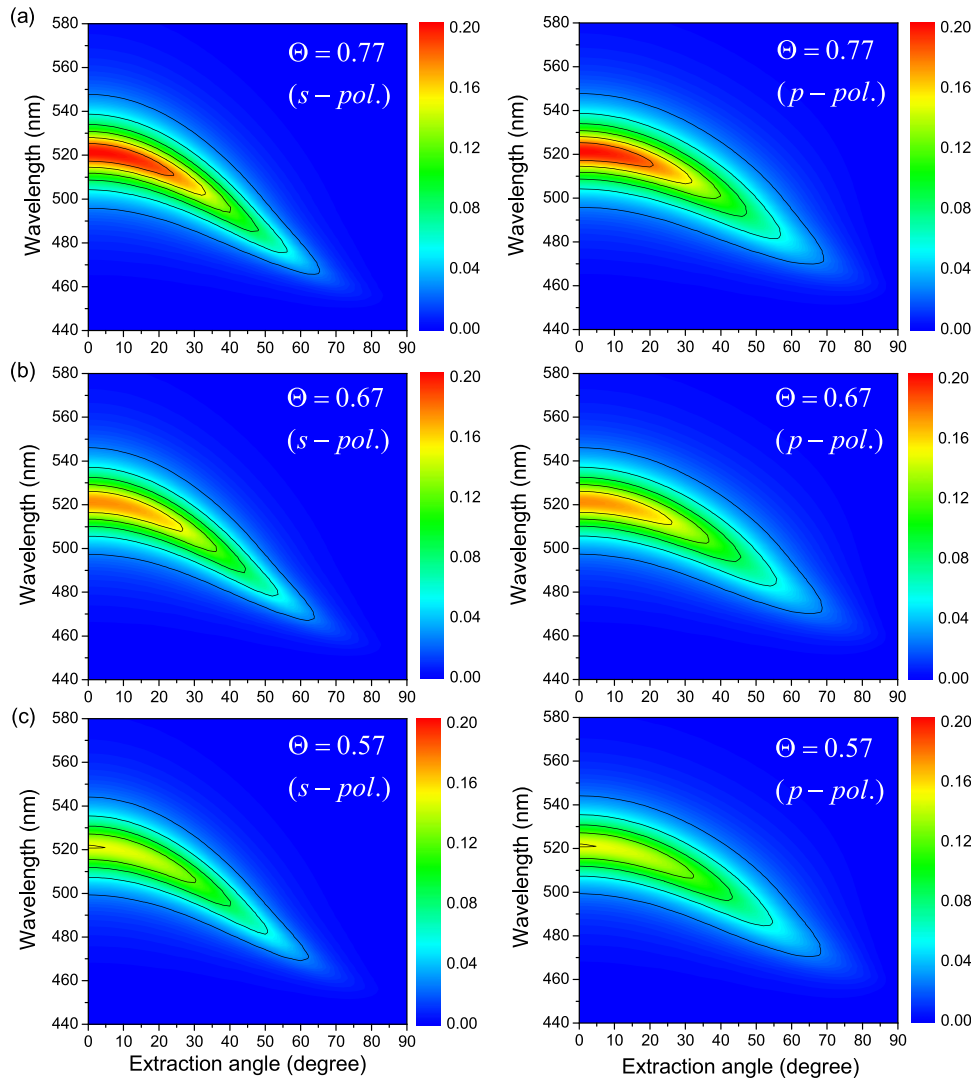
Fig. 8. The 2D-Contour plot of the angular emission spectra depending on the horizontal dipole ratio and light polarization. (a) $\Theta = 0.77$. (b) $\Theta = 0.67$ (isotropic dipole orientation). (c) $\Theta = 0.57$.

proposed generalized Fabry–Pérot formulation was derived based on the source-term method and proven to be equivalent to the currently-used Fabry–Pérot formulation in the case of isotropic dipole orientation. The generalized Fabry–Pérot formulation included all three factors used in the quantum-mechanical model based on Fermi's golden rule.

To demonstrate the applicability and the validity of the generalized Fabry–Pérot formulation, the angular emission characteristics of a top-emitting OLED was calculated with respect to the horizontal dipole ratio and the light polarization. The angular emission spectra became enhanced when the horizontal dipole ratio was high and light is p-polarized, which is matched with previous calculation results obtained by other modeling methods of OLEDs. Because the proposed Fabry–Pérot formulation has a limitation that its application is only limited to the radiation mode, it cannot consider other trapped optical coupling mechanisms such as waveguide modes. However, the generalized Fabry–Pérot formulation has advantage over other electromagnetic models due to its simplicity in the optimization of the multilayer structure of OLEDs, where only the consideration of the radiation mode is sufficient to maximize the output intensity under the micro-cavity effect. The proposed Fabry–Pérot formulation provides an efficient analytical
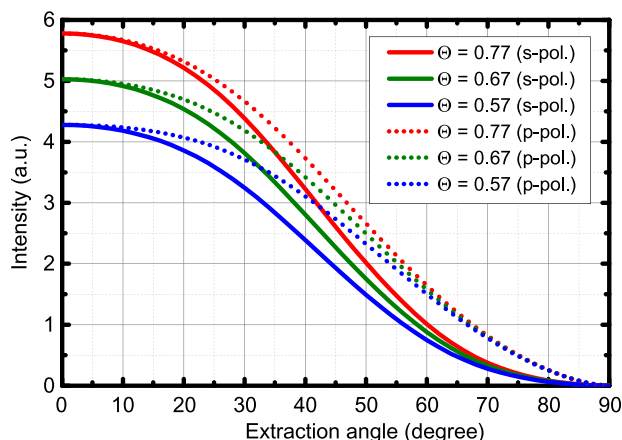
Fig. 9. Calculation results of the total extraction intensity as a function of the extraction angle in various combinations of the horizontal dipole ratio and the light polarization.

method to calculate the effect of the dipole orientation and light polarization in the output characteristics of OLEDs without heavy mathematical and computational complexity.

References

[1] S. Hofmann, M. Thomschke, B. Lüssem, and K. Leo, "Top-emitting organic light-emitting diodes," *Opt. Exp.*, vol. 19, no. S6, pp. A1250–A1264, Nov. 2011.

[2] M. Furno, R. Meerheim, S. Hofmann, B. Lüssem, and K. Leo, "Efficiency and rate of spontaneous emission in organic electroluminescent devices," *Phys. Rev. B, Condens. Matter*, vol. 85, no. 11, Mar. 2012, Art. no. 115205.

[3] S. Tokito, T. Tsutsui, and Y. Taga, "Microcavity organic light-emitting diodes for strongly directed pure red, green, and blue emissions," *J. Appl. Phys.*, vol. 86, no. 5, pp. 2407–2411, Sep. 1999.

[4] C.-L. Lin, H.-W. Lin, and C.-C. Wu, "Examining microcavity organic light-emitting devices having two metal mirrors," *Appl. Phys. Lett.*, vol. 87, no. 2, Jul. 2005, Art. no. 021101.

[5] H. Cho, C. Yun, and S. Yoo, "Multilayer transparent electrode for organic light-emitting diodes: Tuning its optical characteristics," *Opt. Exp.*, vol. 18, no. 4, pp. 3404–3414, Feb. 2010.

[6] M. J. Park *et al.,* "High efficiency red top-emitting micro-cavity organic light emitting diodes," *Opt. Exp.*, vol. 22, no. 17, pp. 19919–19929, Aug. 2014.

[7] J.-S. Kim, P. K. H. Ho, N. C. Greenham, and R. H. Friend, "Electroluminescence emission pattern of organic light-emitting diodes: Implications for device efficiency calculations," *J. Appl. Phys.*, vol. 88, no. 2, pp. 1073–1081, Jul. 2000.

[8] L. H. Smith, J. A. E. Wasey, I. D. W. Samuel, and W. L. Barnes, "Light out-coupling efficiencies of organic light-emitting structures and the effect of photoluminescence quantum yield," *Adv. Funct. Mater.*, vol. 15, no. 11, pp. 1839–1844, Nov. 2005.

[9] S.-Y. Kim *et al.,* "Organic light-emitting diodes with 30% external quantum efficiency based on a horizontally oriented emitter," *Adv. Funct. Mater.*, vol. 23, no. 31, pp. 3896–3900, Aug. 2013.

[10] V. Bulović *et al.,* "Weak microcavity effects in organic light-emitting devices," *Phys. Rev. B*, vol. 58, no. 7, pp. 3730–3740, Aug. 1998.

[11] M. Flämmich *et al.,* "Orientation of emissive dipoles in OLEDs: Quantitative *in situ* analysis," *Org. Electron.*, vol. 11, no. 6, pp. 1039–1046, Jun. 2010.

[12] M. Flämmich *et al.,* "Oriented phosphorescent emitters boost OLED efficiency," *Org. Electron.*, vol. 12, no. 10, pp. 1663–1668, Oct. 2011.

[13] W. Lukosz, "Theory of optical-environment-dependent spontaneous-emission rates for emitters in thin layers," *Phys. Rev. B, Condens. Matter*, vol. 22, no. 6, pp. 3030–3038, Sep. 1980.

[14] K. A. Neyts, "Simulation of light emission from thin-film microcavities," *J. Opt. Soc. Amer. A, Opt. Image Sci.*, vol. 15, no. 4, pp. 962–971, Apr. 1998.

[15] H. Benisty, R. Stanley, and M. Mayer, "Method of source term for dipole emission modification in modes of arbitrary planar structures," *J. Opt. Soc. Amer. A, Opt. Image Sci.*, vol. 15, no. 5, pp. 1192–1201, May 1998.

[16] Z. B. Wang *et al.,* "Optical design of organic light emitting diodes," *J. Appl. Phys.*, vol. 109, no. 5, Mar. 2011, Art. no. 053107.

[17] B. E. A. Saleh and M. C. Teich, *Fundamentals of Photonics*, 2nd ed. Hoboken, NJ, USA: Wiley, 2007.

[18] G. R. Fowles, *Introduction to Modern Optics*, 2nd ed. New York, NY, USA: Dover, 1989.

[19] A. Dodabalapur *et al.,* "Physics and applications of organic microcavity light emitting diodes," *J. Appl. Phys.*, vol. 80, no. 12, pp. 6954–6964, Dec. 1996.

[20] C.-C. Wu, C.-W. Chen, C.-L. Lin, and C.-J. Yang, "Advanced organic light-emitting devices for enhancing display performances," *J. Display Technol.*, vol. 1, no. 2, pp. 248–266, Dec. 2005.

[21] B.-Y. Jung and C. K. Hwangbo, "Determination of an optimized Alq3 layer thickness in organic light-emitting diodes by using microcavity effects," *J. Korean Phys. Soc.*, vol. 48, no. 6, pp. 1281–1285, Jun. 2006.

[22] E. F. Schubert *et al.,* "Highly efficient light-emitting diodes with microcavities," *Science*, vol. 265, no. 5174, pp. 943–945, Aug. 1994.

[23] D. G. Deppe, C. Lei, C. C. Lin, and D. L. Huffaker, "Spontaneous emission from planar microstructures," *J. Mod. Opt.*, vol. 41, no. 2, pp. 325–344, Feb. 1994.

[24] L. A. A. Pettersson, L. S. Roman, and O. Inganäs, "Modeling photocurrent action spectra of photovoltaic devices based on organic thin films," *J. Appl. Phys.*, vol. 86, no. 1, pp. 487–496, Jul. 1999.

[25] J. Kim, S. Jung, and I. Jeong, "Optical modeling for polarization-dependent optical power dissipation of thin-film organic solar cells at oblique incidence," *J. Opt. Soc. Korea*, vol. 16, no. 1, pp. 6–12, Mar. 2012.

[26] G. He *et al.,* "High-efficiency and low-voltage p-i-n electrophosphorescent organic light-emitting diodes with double-emission layers cells," *Appl. Phys. Lett.*, vol. 85, no. 17, pp. 3911–3913, Oct. 2004.

[27] S. Mladenovski *et al.,* "Integrated optical model for organic light-emitting devices," *J. Appl. Phys.*, vol. 109, no. 8, Apr. 2011, Art. no. 083114.

[28] C. C. Katsidis and D. I. Siapkas, "General transfer-matrix method for optical multilayer systems with coherent, partially coherent, and incoherent interference," *Appl. Opt.*, vol. 41, no. 19, pp. 3978–3987, Jul. 2002.

[29] S. Jung *et al.,* "Optical modeling and analysis of organic solar cells with coherent multilayers and incoherent glass substrate using generalized transfer matrix method," *Jpn. J. Appl. Phys.*, vol. 50, no. 12, Dec. 2011, Art. no. 122301.

[30] K. Kang, S. Lee, and J. Kim, "Effect of an incoherent glass substrate on the absorption efficiency of organic solar cells at oblique incidence analyzed by the transfer matrix method with a glass factor," *Jpn. J. Appl. Phys.*, vol. 50, no. 5, May 2013, Art. no. 052301.

[31] S. Lee *et al.,* "Effect of incidence angle and polarization on the optimized layer structure of organic solar cells," *Sol. Energy Mater. Sol. Cells*, vol. 118, pp. 9–17, Nov. 2013.

[32] S. L. Chuang, *Physics of Photonic Devices*, 2nd ed. Hoboken, NJ, USA: Wiley, 2009.

[33] E. F. Schubert, *Light-Emitting Diodes*, 2nd ed. New York, NY, USA: Cambridge Univ. Press, 2006.

[34] H. Benisty, H. De Neve, and C. Weisbuch, "Impact of planar microcavity effects on light extraction—Part I: Basic concepts and analytical trends," *IEEE J. Quantum Electron.*, vol. 34, no. 9, pp. 1612–1631, Sep. 1998.

[35] K. Kang, J. Yoon, J. Kim, H. Lee, and B. Yang, "Effect of the finite pixel boundary on the angular emission characteristics of top-emitting organic light-emitting diodes," *Opt. Exp.*, vol. 23, no. 11, pp. A709–A717, May 2015.

[36] P. A. Hobson, J. A. E. Wasey, I. Sage, and W. L. Barnes, "The role of surface plasmons in organic light-emitting diodes," *IEEE J. Sel. Topics Quantum Electron.*, vol. 8, no. 2, pp. 378–386, Mar./Apr. 2002.

[37] [Online]. Available: http://refractiveindex.info.

[38] H.-W. Lin *et al.,* "Anisotropic optical properties and molecular orientation in vacuum-deposited ter(9,9-diarylfluorene)s thin films using spectroscopic ellipsometry," *J. Appl. Phys.*, vol. 95, no. 3, pp. 881–886, Feb. 2004.